Applied Ocean Research 154 (2025) 104428

Contents lists available at ScienceDirect

Applied Ocean Research

journal homepage: www.elsevier.com/locate/apor

Control of nonlinear offshore platforms using semi-active tuned mass damper inerter under combined wave and wind loads

Seyyed Ali Mousavi Gavgani [a], Seyed Hossein Hosseini Lavassani [a,*], Gebrail Bekdaş [b]

[a] Department of civil engineering, Faculty of Engineering, Kharazmi University, Tehran, Iran
[b] Department of Civil Engineering, Istanbul University-Cerrahpas, Avcılar, Istanbul, Turkey

ARTICLE INFO

Keywords:
Offshore platform
Semi-active Tuned mass damper Inerter (SATMDI)
Interval type-2 fuzzy logic controller (IT2FLC)
Bouc-Wen hysteretic model
Fluid-structure interaction (FSI)
Nonlinear structure

ABSTRACT

The present paper investigates the effectiveness of a new control system called Semi-Active Tuned Mass Damper Inerter (SATMDI) in mitigating vibrations of offshore platforms with nonlinear behavior subjected to simultaneous wind and wave loading with various return periods. This new control system is specifically evaluated on Ressalat jacket platform and this study considers the fluid-structure interaction (FSI) in addition to the added mass effect because of platform oscillation in the fluid. An interval type-2 fuzzy logic controller (IT2FLC) is used for online voltage calculation of this control system. The utilized IT2FLC is optimized with an algorithm called the observer-teacher-learner-based optimization (OTLBO). Additionally, the hysteretic behavior of the platform is simulated by means of the Bouc-Wen model. The results indicate that the proposed optimal control SATMDI + IT2FLC can significantly dissipate a considerable amount of energy applied to the structure, therefore avoid the structure from entering the plastic range. For instance, under a loading scenario with a 100-year return period, the decrease in maximum inter-story drift and absolute acceleration responses are estimated about 91 % and 83 %, respectively.

Nomenclature

Symbol	Meaning	Symbol	Meaning
N	Number of degrees of freedom (DOF)	C	Total damping matrix
i	Each level of the structure	c_i	Damping of each level of the structure
M	Total mass matrix	c_d	Damping of the damper
M_0	Structural mass matrix	$\varphi(x,t)$	Nonlinear restoring force vector
M_a	Added mass matrix	$x(t)$	Interstory drift vector
M_{tot}	Sum of the structural mass	x_i	Interstory drift of each level
m_i	Mass of each level of the structure	x_d	Interstory drift of damper
m_d	Mass of the damper	$z'(t)$	Displacement vector of the nonlinear element
b	Inertance coefficient of the inerter	α_i	Ratio of the post yielding to pre-yielding stiffness
ib	Connected DOF to one end of inerter	D'_{y_i}	Yield deformation in the hysteresis behavior of the structure
K_{el}	Total elastic stiffness matrix	P'_i	Quantity for control the shape of the structural hysteretic loop
K_{in}	Total inelastic stiffness matrix	λ'_i	Quantity for control the shape of the structural hysteretic loop
k_i	Linear stiffness of each level of the structure	ψ'_i	Quantity for control the shape of the structural hysteretic loop
k_i^{el}	Elastic stiffness of each level of the structure	n'_i	Quantity for regulate the smoothness of the structural force-deformation curve
k_i^{in}	Inelastic stiffness of each level of the structure	μ	Mass ratio of damper
k_d	Linear stiffness of the damper	β	Inertance ratio of damper

(continued on next page)

* Corresponding author.
E-mail address: lavassani@khu.ac.ir (S.H.H. Lavassani).

https://doi.org/10.1016/j.apor.2025.104428
Received 2 October 2024; Received in revised form 12 December 2024; Accepted 10 January 2025

(*continued*)

k_d^{el}	Elastic stiffness of the damper	γ	Frequency ratio of damper
k_d^{in}	Inelastic stiffness of the damper	ζ	Damping ratio of damper
ω_d	Damper frequency	U	Wave particle velocity
$\omega_{s(1)}$	Primary structural system frequency	$\dot{U}$	Wave particle acceleration
ω_f	Circular frequency of the structure	U_w	Static or mean wind speed
F_I	Inertia force	$u_w(t)$	Fluctuating wind speed
F_D	Drag force	u_*	Friction velocity
F_W	Wind-induced force	$U(H)$	Mean wind speed at height H
F_C	Control force	$S_{rr}(H,\omega_f)$	Power spectral density function (PSDF) at height $H$for the frequency ω_f
V	Volume vector of the structural members	u	Voltage applied to MR damper
A	Cross-sectional area vector of the structural members	v	MR damper command voltage
$\circ$	Element-wise product	ρ_w	Water density
S	Area exposed to the wind flow	ρ_a	Air density
H	Height of the structure	C_m	Water inertia coefficient
$Y_p\left(k_f\Delta f_f\right)$	Complex random numbers	C_d	Water drag coefficient
R	Total number of points used for the simulation	C_D	Air drag coefficient
k_f	Running random frequencies	Λ	Position vector of the control force
r	Integers from 0 to R	$\dot{y}$	Relative velocity between MR damper ends
E	Expectation operator	α_{MR}	Hysteretic stiffness of MR damper
f_{fc}	Cut-off nyquist frequency	α_a	Hysteretic stiffness at off state of MR damper
$y_p(r\Delta t)$	Discrete frequency function of the wind speed	α_b	Voltage dependent hysteretic stiffness of MR damper
$H_{pi}\left(k_f\Delta f_f\right)$	Lower triangular matrix resulted from Cholesky decomposition of the PSDF	c_0	Viscous damping coefficient of MR damper
ε_{ik}	Complex Gaussian random number	c_{0a}	Viscous damping coefficient at off state of MR damper
ξ_{ik}	Real part of complex number	c_{0b}	Voltage dependent viscous damping coefficient of MR damper
η_{ik}	Imaginary part of complex number	D	Quantity for control the shape of the MR damper hysteretic loop
p	Size of the Cholesky matrix	ψ	Quantity for control the shape of the MR damper hysteretic loop
T	Delay constant	λ	Quantity for control the shape of the MR damper hysteretic loop
z	Hysteretic evolutionary variable	n	Quantity for control the shape of the MR damper hysteretic loop
E_U	Area under the uncontrolled hysteresis curve	E_C	Area under the controlled hysteresis curve

1. Introduction

Offshore structures, unlike their onshore counterparts, are subjected to a wide range of severe environmental loads due to their unique locations. Over the years, this has resulted in significant structural and non-structural damages. For example, Fig. (1) illustrates some of these damages experienced by real offshore platforms, where certain structural elements have exhibited nonlinear behavior. Statistics reveal that storms such as Ike in 2008, and Katrina and Rita in 2005, led to the destruction of numerous platforms and caused substantial damage, sometimes even triggering global oil crises (Paganie, 2008). This issue is not confined to past decades; for instance, in 2021, a similar incident occurred due to Ida Hurricane. These statistics demonstrate that even in recent years, offshore structures have not been immune to environmental forces and have sustained damage. Therefore, the importance of researching and implementing techniques to mitigate vibrations in these types of structures and prevent nonlinear behaviors is more evident than ever. In general, to reduce vibrations caused by dynamic loads, two approaches can be employed: increasing structural capacity or reducing the demand on the structure. Various studies on different structures have shown that employing structural control methods to reduce demand can be highly effective and has fewer negative consequences compared to capacity-increasing approaches (Soong and Dargush, 1997; Gavgani et al., 2021).

The available methods for controlling the response of structures are categorized into four categories, namely passive, active, semi-active, and hybrid (Farzam et al., 2020). These methods have evolved and improved over time to address the shortcomings of their predecessors, leading to the development of more sophisticated and optimized control systems (Jalali et al., 2023). For example, the Tuned Mass Damper (TMD) is a widely recognized passive control device, first introduced by Frahm in 1909 (Singh et al., 2002). The effectiveness of TMDs in mitigating offshore platform vibrations was first evaluated by Abdel-Rohman in 1996 (Abdel-Rohman, 1996). The performance of a TMD hinges on the precise tuning of its parameters relative to the uncontrolled structure, allowing it to absorb and dissipate a substantial portion of the structure's energy. Furthermore, research has demonstrated that the efficacy of TMDs in safeguarding civil structures is highly dependent on their inertia properties (Hoang et al., 2008; Moutinho, 2012). Practically, the larger the mass of the TMD, the more effective it is in vibration control (De Angelis et al., 2012). Therefore, researchers have proposed unconventional large-mass TMDs, where the top story (or several top stories) is connected to the lower stories via isolators, enabling the upper stories to function as an additional TMD mass (Matta and De Stefano, 2009). In such cases, the TMD mass can reach up to 50 % or more of the total mass of the structure (Giaralis and Taflanidis, 2018). However, this approach is not only costly in terms of design and implementation but also increases uncertainties and complexities during the design and tuning process. This complexity arises from the nonlinear behavior of the isolators under strong ground motions. Additionally, some researchers have attempted to distribute multiple TMDs throughout the structure, though this approach has not fully resolved the previous challenges (Wang and Lin, 2005). These persistent challenges have ultimately led to the introduction of a novel concept known as the inerter.

The inerter idea was introduced by Smith at the University of Cambridge in 2002 for the first time (Smith, 2002). Following this, various theories and mechanical devices under the name inerter were developed by other researchers, including ball-screw (Den Hartog, 1956), rack and pinion (Marian and Giaralis, 2014), helical fluid (Ruiz et al., 2018), gyro-mass damper (Saitoh, 2012), living-hinge (John and Wagg, 2019), hydraulic inerter (Wang et al., 2011) and etc. (Su et al., 2024). The successful application of these devices in Formula 1 car suspensions (Lazar et al., 2014) and train suspension systems (Wang et al., 2009) quickly increased the popularity of the inerter due to its efficiency and advantages. Subsequently, various control devices based on the inerter were introduced, such as the electromagnetic inertial mass damper (Zhu et al., 2019), rotational inertia viscous damper (Hwang et al., 2007), tuned inerter damper (Lazar et al., 2014), series-parallel inerter system (Zhang et al., 2020), inerter-based dynamic vibration absorbers (Hu et al., 2018) and etc. Marian and Giaralis conceptualized a new damper, the Tuned Mass Damper Inerter (TMDI), by series combining an inerter

Fig. 1. Examples of offshore platform damages caused by environmental forces. a) EI-322-A platform during the Lili Hurricane in 2002 (DeFranco et al., 2004); b) Thunder Horse platform during the Dennis Hurricane in 2005 (Kelessidis, 2009); c) Mars platform during the Katrina Hurricane in 2005 (Kaiser and Pulsipher, 2007); d) Ocean Warwick platform during Katrina Hurricane in 2005 (Kaiser and Pulsipher, 2007).

with a TMD (Marian and Giaralis, 2014). They considered it an efficient alternative to the classical TMD in mitigating civil structures' vibrations. The TMDI achieves better performance with significantly reduced mass compared to classical large-mass TMDs by quickly converting linear motion into rotational motion (Giaralis and Marian, 2016). Essentially, the inerter can achieve an inertia magnitude several times greater than its physical mass (Zhu et al., 2019). This was experimentally demonstrated by Chen and colleagues, who achieved an inertance of 60 to 240 kg with a 1-kg inerter (Chen et al., 2009). Numerous numerical and experimental studies have emphasized the favorable effect of adding inerters to traditional control devices (Sun et al., 2019; Pietrosanti et al., 2021; Ma et al., 2021; Su et al., 2022). The first study on the control of offshore platform responses using the inerter-based devices was conducted by Ma et al. in 2018. They utilized a tuned heave plate equipped with inerter to mitigate the vibrations of a semi-submersible platform (Ma et al., 2018). In 2020, Ma et al. repeated this study using a vibration isolation system with inerter along with a rotational inertia damper (Ma et al., 2020; Ma et al., 2020). In 2023, Xu et al. studied the performance of a damper of tuned inerter type to control vibrational responses of a jacket platform (Xu et al., 2023). Zhao et al. introduced the inerter nonlinear energy sink and evaluated its effectiveness in the vibration control of a jacket platform (Zhao et al., 2023). Additionally, Ma et al. in 2023 combined conventional bearings with inerter-based dampers to introduce a novel device called the inerter-based damping isolation system, which they tested on a platform (Ma et al., 2023). All these introduced control devices are categorized as passive control systems. Numerous studies on various structures have demonstrated that passive control systems often exhibit limited and sometimes suboptimal performance in dissipating the applied energy to the structure (Enferadi et al., 2019; Fahimi Farzam et al., 2021). To address these limitations, a semi-active TMD equipped with an inerter can be employed. In this control system, the parameters of the inerter-based damper adjust in real time according to the input excitation. They evaluated the performance of their innovative control system on a jacket platform with linear behavior and demonstrated the superiority of the semi-active SATMDI over the passive TMDI. Due to its structural similarity to the classical TMD, this damper is likely to attract significant attention from researchers in the field of platform control and see widespread implementation in real structures.

According to the literature review, research on the application of inerters in control systems for reducing vibrations in offshore platforms is very limited. Notably, only one study has focused on TMDI and the semi-active control of inerter-based dampers for platform vibration mitigation. Furthermore, many of the performed investigations on the controlling vibration of offshore platforms have assumed linear structural response, including all those related to inerter-based control systems. Thus, this research aims to evaluate the effectiveness of the novel SATMDI damper in reducing vibrations and dissipating energy in a jacket platform while accounting for the nonlinear structural responses. In addition to the innovations mentioned, this study features several key aspects: (1) The Bouc-Wen hysteresis model is utilized to account for the nonlinear response of the platform. (2) The offshore platform is subjected to simultaneous wind and wave loading with various return periods. (3) The use of interval type-2 fuzzy logic controller (IT2FLC), which was optimized employing of the Observer-Teacher-Learner-Based Optimization (OTLBO) algorithm, and includes actuator saturation effect, addresses a significant practical issue in semi-active control systems. (4) The added mass resulting from platform vibrations in the fluid is calculated in real time. (5) Fluid-structure interaction (FSI) is considered to achieve more realistic results. (6) A novel method is employed for generating wave forces acting on the platform. (7) Responses are presented in a dimensionless form to ensure generalizability to other scenarios. By integrating these aspects, the study aims to provide a comprehensive evaluation of the SATMDI's performance under realistic and challenging conditions, thereby contributing valuable insights to the field of offshore platform vibration control.

2. Motion equation of nonlinear structure with SATMDI

In contrast to linear structures, which exhibit constant stiffness over time, defining the structural restoring force model to determine the stiffness at each moment is imperative for nonlinear structures. Therefore, when modeling a shear-type lumped mass structure with nonlinear behavior, the utilization of a Bouc-Wen hysteresis element in conjunction with spring and damper elements, as illustrated in Fig. (2), becomes essential (Yuan et al., 2024). Based on this premise, the equation of motion for a platform with N degrees of freedom (dof), featuring hysteretic behavior and controlled by an SATMDI located on top of the first level subjected to dynamic forces as well as the control input is given by Eq. (1).

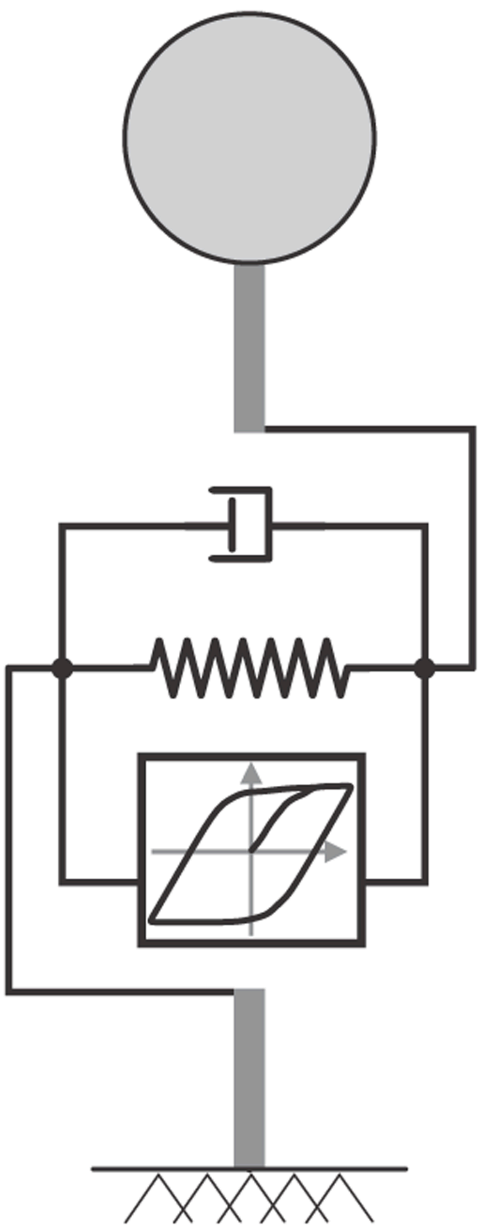

Fig. 2. Schematic illustration of the nonlinear behavior modeling concept for a single-degree-of-freedom (SDOF) shear-type structure.

$$M\ddot{x}(t) + C\dot{x}(t) + \varphi(x,t) = F_I + F_D + F_W + F_C \tag{1}$$

where M and C are symmetric mass and damping matrices of dimension $(N+1)\times(N+1)$, are computed according to Eqs. (2) and (3), wherein all elements except those with numerical values are zero (Giaralis and Petrini, 2017). Notably, the utilized mass matrix consists of the mass of the structure and the damper (M_0) and the added mass (M_a), as explained below. $\varphi(x,t)$ signifies the nonlinear restoring force vector with dimension $(N+\ 1)\times\ 1$, portraying the structure's hysteretic behavior and described using the Bouc-Wen model according to Eq. (4) (Yang et al., 1996). Additionally, $x(t)$ in Eq. (1) stands for the inter-story drift vector of dimension $(N+\ 1)\times\ 1$, structured as $x(t) = [x_1, x_d, x_2, \ldots, x_N]^T$.

$$M_0 = \begin{bmatrix} m_1 & & & & & \\ & m_d + b & \cdots & \cdots & -b & \\ & & m_2 & & \vdots & \\ & & & \ddots & \vdots & \\ & & & & m_{ib} + b & \\ & & & & & \ddots & \\ SYM & & & & & & m_N \end{bmatrix} \tag{2}$$

$$C = \begin{bmatrix} c_1 + c_2 + c_d & -c_d & -c_2 & & \\ & c_d & & & \\ & & c_2 + c_3 & -c_3 & \\ & & & \ddots & -c_N \\ SYM & & & & c_N \end{bmatrix} \tag{3}$$

$$\varphi(x,t) = K_{el}x(t) + K_{in}z'(t) \tag{4}$$

where m_i and c_i and m_i for $i = 1,\ldots,N$ represent the damping and mass, respectively at each mass level of the platform, respectively. Moreover, m_d and c_d denote the mass and damping matrices of the damper placed on the first platform level. In addition, b in Eq. (2) stands as an inherent feature of the TMDI damper known as inertance, influencing only the mass matrix, and ib designates the degree of freedom connected to an inerter terminal. Essentially, an inerter is a mechanical device with two terminals generating a resisting force proportional to the relative acceleration at its ends (Dai et al., 2021). In Eq. (4), the parameters K_{el} and K_{in} symbolize the symmetric $(N+1)\times(N+1)$ stiffness matrices in the elastic and inelastic states given by Eqs. (5) and (6) (Temimi et al., 2016). Furthermore, $z'(t)$ represents the hysteretic component of the restoring force (the displacement vector of the nonlinear element), derived through Eq. (7).

$$K_{el} = \begin{bmatrix} k_1^{el} + k_2^{el} + k_d^{el} & -k_d^{el} & -k_2^{el} & & \\ & k_d^{el} & & & \\ & & k_2^{el} + k_3^{el} & -k_3^{el} & \\ & & & \ddots & -k_N^{el} \\ SYM & & & & k_N^{el} \end{bmatrix}; k_i^{el} = \alpha_i k_i \tag{5}$$

$$K_{in} = \begin{bmatrix} k_1^{in} + k_2^{in} + k_d^{in} & -k_d^{in} & -k_2^{in} & & \\ & k_d^{in} & & & \\ & & k_2^{in} + k_3^{in} & -k_3^{in} & \\ & & & \ddots & -k_N^{in} \\ SYM & & & & k_N^{in} \end{bmatrix}; k_i^{in} = (1-\alpha_i)k_i D'_{y_i} \tag{6}$$

$$\dot{z}'_i(t) = \left(D'_{y_i}\right)^{-1}\left[P'_i\dot{x}_i - \lambda'_i|\dot{x}_i|z'_i|z'|^{n'_i-1} - \psi'_i\dot{x}_i|z'|^{n'_i}\right] \tag{7}$$

The parameters k_i^{el} and k_i^{in} respectively denote the elastic and inelastic stiffness of level i of the structure. Eqs. (5) and (6) outline the computation of these stiffness values for each mass level, necessitating the linear stiffness of the desired level k_i, the ratio of the post-yielding stiffness of the desired level to its stiffness before yielding α_i, and also the yielding deformation of the considered level D'_{y_i}. Furthermore, k_d^{el} and k_d^{in} in Eqs. (5) and (6) respectively represent the elastic and inelastic stiffness of the damper. Eq. (7) introduces constants P'_i, λ'_i, ψ'_i, and n'_i, governing the hysteresis loop's characteristics associated with nonlinear behavior of i^{th} level, detailed in Quaranta et al. study (Quaranta et al., 2016). Based on the Ikhouane and Rodellar research, these parameters have been categorized into five distinct classes (Ikhouane and Rodellar, 2007). Among them, it has been demonstrated that class I ($P'_i > 0, \lambda'_i + \psi'_i > 0, and \lambda'_i - \psi'_i \geq 0$) is the only category that satisfies several critical conditions: BIBO stability, compatibility with the free motion of real systems modeled by Bouc–Wen, and adherence to thermodynamic principles. As such, class I is the sole category relevant for accurately representing physical phenomena, and it is the focus of this study. Accordingly, the selection of Bouc–Wen parameters in this study was guided by these principles. For their specific values, references from existing literature were consulted to ensure physical relevance and adherence to established guidelines. For a clearer insight, Fig. (3) illustrates a force-displacement diagram depicting a hysteresis loop and some of the influential parameters.

In order to design an appropriate TMDI, it is essential to determine parameters including the mass ratio (μ), the inertance ratio (β), the frequency ratio (γ), and the damping ratio (ζ), as defined by Eq. (8) (Djerouni et al., 2021).

$$\beta = \frac{b}{M_{tot}}; \mu = \frac{m_d}{M_{tot}}; \gamma = \frac{\omega_d}{\omega_{s(1)}} = \frac{\sqrt{\frac{k_d}{(m_d+b)}}}{\omega_{s(1)}}; \zeta = \frac{c_d}{2\sqrt{(m_d+b)\times k_d}} \tag{8}$$

where M_{tot}, ω_d, and $\omega_{s(1)}$ respectively denote the total structural mass, the frequency of the TMDI damper, and the fundamental frequency of the structure.

In Eq. (1), F_I and F_D represent the inertia and drag forces, derived from the Morison equation as per Eqs. (9) and (10) (Dastan Diznab et al., 2016). Additionally, F_W denotes wind load, calculated according to Bernoulli's theory expressed in Eq. (11) (Banerjee et al., 2022). Finally, F_C signifies the applied control force produced by the magneto-rheological damper.

$$F_I = \rho_w C_m V \circ \dot{U} \tag{9}$$

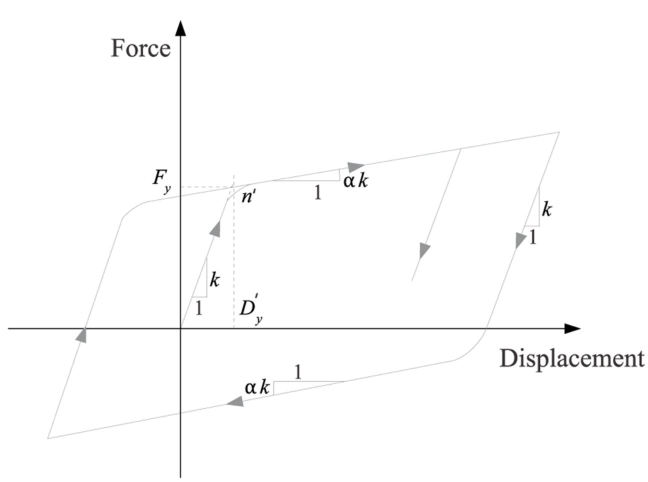

Fig. 3. Force-displacement diagram illustrating the nonlinear material behavior of the structure with introduced parameters affecting it (Bigdeli et al., 2014).

$$F_D = \rho_w C_d A' \circ (U - \dot{x}) \circ |U - \dot{x}| \tag{10}$$

$$F_W = \frac{1}{2}\rho_a S C_D [U_w + u_w(t)]^2 \tag{11}$$

In Eqs. (9) and (10), U and $\dot{U}$ stands for the wave velocity and wave acceleration, respectively, while ρ_w denotes water density assumed to be equal to 1024 kg/m³. Moreover, C_m and C_d are the inertia and drag coefficients related to the wave force, considered as 1.2 and 1.05 following API regulations (Rp2A-Wsd, A 2007). Furthermore, V and A represent the vectors of the elements' volume and cross-section area. Additionally, the symbol "∘" denotes the element-wise product operator. In Eq. (11), ρ_a represent the air density, which is taken equal to 1.25 kg/m³. Additionally, S represents the windward surface area of the structure. Moreover, C_D is the wind force drag coefficient, which is assumed to be 1 for platforms based on the API requirements (Rp2A-Wsd, A 2007).

In Eq. (11), U_w and $u_w(t)$ represent the mean and fluctuating speeds of the wind along the longitudinal direction, where the former is independent of time, and the latter varies with time. The wind speed profile over time is composed of both the mean and fluctuating wind speeds. For dynamic analyses, the fluctuating speed is calculated based on the maximum gust speed (measured at an elevation of 10 m above ground level) using an online application developed by Kwon and Kareem (Kwon and Kareem, 2006). For this purpose, the power spectral density function (PSDF) proposed by Kaimal et al. (Kaimal et al., 1972) and Simiu (Simiu, 1974) for the longitudinal wind speed fluctuations is utilized. This PSDF is defined as follows in Eq. (12):

$$S_{rr}(H, \omega_f) = \frac{1}{2}\frac{200}{2\pi}u_*^2\frac{H}{U(H)}\frac{1}{\left[1 + 50\frac{\omega_f H}{2\pi U(H)}\right]^{5/3}} \tag{12}$$

in which, H, ω_f, u_*, and $U(H)$ denote the height of the structure, the angular frequency, the frictional velocity, and the mean wind speed at elevation $H$from the base level, respectively. To produce the time histories, using the Fast Fourier Transform (FFT) proposed by Witting and Sinha (Wittig and Sinha, 1975) and taking advantage of the discrete frequency function along the height of the structure. The discrete time series points are replicated by Eq. (13) (Elias et al., 2019).

$$y_p(r\Delta t) = \frac{1}{R}\sum_{k_f=0}^{R} Y_p\left(k_f \Delta f_f\right)\exp\left(j\frac{2\pi k_f r}{R}\right) \tag{13}$$

In Eq. (13), $Y_p\left(k_f \Delta f_f\right)$ represents random complex numbers, produced from a set of completely independent Gaussian random numbers. Additionally, R denote the total number of points used for simulation. k_f and r are also, the running random frequencies, and integers in the range of 0 to R, respectively. Eq. (14) gives the Gaussian random numbers.

$$\varepsilon_{ik} = \xi_{ik} + j\eta_{ik} \tag{14}$$

In Eq. (14), $E[\xi_{ik}] = E[\eta_{ik}] = 0$ and $E[\xi_{ik}^2] = E[\eta_{ik}^2] = 0.5$, where E denotes the expectation operator. Consequently, Eq. (13) will be rewritten as Eq. (15).

$$Y_p\left(k_f \Delta f_f\right) = \sum_{i}^{p} H_{pi}\left(k_f \Delta f_f\right)\varepsilon_{ik} \times \sqrt{2 f_{fc} R} \tag{15}$$

where $H_{pi}\left(k_f \Delta f_f\right)$ is the lower triangular matrix derived from the Cholesky decomposition of the power spectral density function $S\left(f_f\right)$. f_{fc} in Eq. (15) represents the cut-off Nyquist frequency. The size of the Cholesky matrix is equal to $p = 1to200$ (Bhattacharya and Dalui, 2022). The optimal cut-off frequency is set as the fundamental frequency of the structure to yield the maximum possible response (Baheti and Matsagar, 2022).

As mentioned previously, the mass matrix M in Eq. (1) is equal to the summation of the added and the structural masses, M_a and M_0, as specified by Eq. (16). The concept of added mass considers the additional mass of water surrounding the platform, which becomes dynamically incorporated into the system as the platform accelerates under wave-induced forces. This added mass exerts a reactive force on the platform, opposing its direction of motion. The added mass is derived from Eq. (17) (Lavassani et al., 2023).

$$M = M_0 + M_a \tag{16}$$

$$M_a = \rho(C_m - 1)V \tag{17}$$

According to Eq. (18), the Bouc-Wen model is used to calculate the generated control force by the MR damper (Ok et al., 2007).

$$F_C = \Lambda(c_0\dot{y} + \alpha_{MR}z) \tag{18}$$

where the control force position vector is characterized by Λ, and $\dot{y}$ is the relative velocity at the damper's ends. Moreover, the hysteresis deformation z characterizes a path-dependent response obtained from Eq. (19).

$$\dot{z} = -\lambda|\dot{y}|z|z|^{n-1} - \psi\dot{y}|z|^n + D\dot{y} \tag{19}$$

In Eq. (19), D, ψ, λ, and n stand for the parameters that adjust the damper's response curve shape. Furthermore, α_{MR} and c_0 (representing the damper's viscous damping) can be derived as a function of the effective voltage, u, according to Eqs. (20) and (21).

$$\alpha_{MR} = \alpha_a + \alpha_b u \tag{20}$$

$$c_0 = c_{0a} + c_{0b}u \tag{21}$$

where c_{0a}, c_{0b}, α_a, and α_b account for the dependency of the force of MR damper on the applied voltage. In these equations, u is computed according to the first-order filter according to Eq. (22) in order to model the MR fluid dynamics to attain rheological equilibrium, where v is the voltage generating the current, determined using a type-2 fuzzy controller.

$$\dot{u} = -\mathrm{T}(u - v) \tag{22}$$

in Eq. (22), T is the time constant in the first-order filter.

3. Design of optimum interval type-2 fuzzy logic controller

In the present study, an interval type-2 fuzzy logic controller (IT2FLC) is employed to calculate the appropriate control voltage in real time for controlling platform vibrations. This advanced fuzzy system evolved from type-1 fuzzy systems, first introduced by Zadeh in 1975 (Zadeh, 1975). Type-2 fuzzy systems gained prominence because of the limitations of type-1 fuzzy systems in handling uncertainties, with numerous studies validating their high efficiency (Du et al., 2020; Al-Ghazali and Shariatmadar, 2021). Fuzzy logic, in general, uses linguistic expressions to compute outputs, considering a range of values instead of a single deterministic number for the input and output variables. This approach allows fuzzy logic to account for uncertainties within the structure, such as noise and time delay, and capture the nonlinearities of structural performance. Hence, IT2FLC is employed in this study to accommodate the nonlinear behavior of the structure.

As illustrated in Fig. (4), a type-2 fuzzy system comprises an input processing, the inference system, and an output processing. During input processing, specific membership functions are used to fuzzify the deterministic data, which is mapped onto fuzzy sets. In the next step, the data is fed to the inference system, where various fuzzy rules are combined to map the input fuzzy sets to the output. Among the various inference systems, the Mamdani inference system is particularly popular because of its straightforwardness and intuitive nature. In the final step, the determined fuzzy output needs to be converted into deterministic values during output processing. This involves a two-step process in type-2 fuzzy systems. The first step, known as type-reduction, converts a fuzzy set from type-2 into a type-1 set. Several approaches for type-reduction have been suggested by investigators, with the method called Center of Sets (COS) being preferred for its simplicity (Karnik and Mendel, 1998). The next step includes the defuzzification of the reduced set into a deterministic value using output membership functions.

The designed controller features two inputs, the displacement and velocity of the specified structure level, and one output. In this study, five membership functions (MF) with triangular shapes are utilized within the range of $[-1 \quad 1]$ to fuzzify the input data. It is worth noting that an odd number of MFs is selected to eliminate the zero positive and negative fuzzy sets (Cheong and Lai, 2000). Triangular MFs are favored because of their lower computational complexity and superior performance compared to other shapes (Singh et al., 2022). Given the input membership functions' range, the displacement and velocity values of

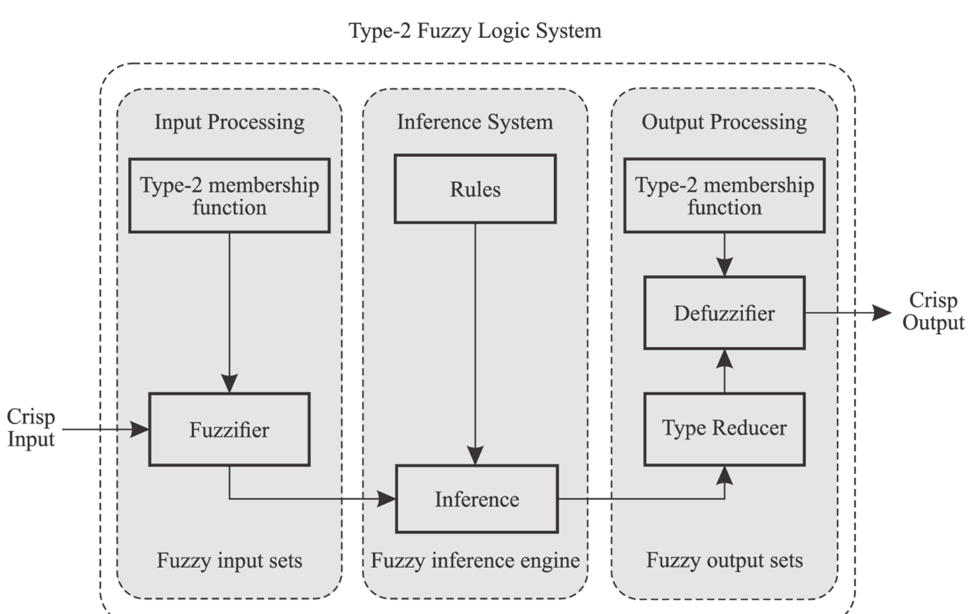

Fig. 4. Structure of an Interval Type-2 Fuzzy System.

the specified level are normalized to the maximum uncontrolled values at that level. Considering the number of fuzzy controller inputs and their related membership functions, 25 control rules are employed in this study. For defuzzifying the fuzzy controller output, seven triangular MFs are utilized, with a range of $[0 \quad 10]$ according to the input voltage range of the MR damper.

The determination of the shape, number, and arrangement of the MFs for the inputs and output is empirical and trial-based. Consequently, some studies employ metaheuristic algorithms for this purpose. For instance, Pourzeynali et al. optimized the architecture of input and output MFs using a genetic algorithm, demonstrating that it could enhance the controller's performance (Pourzeynali et al., 2007). Therefore, in this research, the input and output MFs and fuzzy rules are optimized taking advantage of the observer-teacher-learner-based optimization (OTLBO) algorithm. This algorithm, proposed by Shahrouzi et al. in 2017, is based on the principles of evolutionary computation and the Teaching-Learning-Based Optimization (TLBO) algorithm (Shahrouzi et al., 2017). A summary of the steps of the OTLBO algorithm is illustrated in Fig. (5).

For optimizing the MFs, the method suggested by Park et al. is adopted, which leverages the symmetrical performance of most dynamic systems, counting controlled structures (Park et al., 1995). Consequently, the input MFs are considered symmetric about the vertical axis. In Type-2 fuzzy sets, an upper and a lower MFs are present (UMF and LMF), where for all input values, the LMF can be less than or equal to the UMF. To manage the uncertainty, the area between these two series of MFs is defined as the footprint of uncertainty (FOU). The optimization of the input and output MFs involves defining the longitudinal coordinates of the triangular functions' central vertices. An important point to consider is that the vertices' longitudinal coordinates on the left and right sides of each triangular function should align with the central vertex's longitudinal coordinate of the adjacent triangular function.

To achieve an optimal controller, the fuzzy rules applied in the inference system must also be optimized. The fuzzy rule base is designed and then fine-tuned to maximize compatibility between input and output values. For example, because of the symmetry in the MFs, the fuzzy rules should also exhibit symmetry and be paired accordingly. Therefore, one can optimize one-half of the fuzzy rules arranged based on the MFs in a table and derive the rest based on the symmetry concept. As mentioned earlier, the current research employs 25 fuzzy rules, and optimizing them involves consideration of 12 variables. Following optimization, 24 control rules are determined, with one rule remaining. This additional rule exclusively addresses the initial states, specifically zero displacement and also zero velocity, where the control voltage is set to zero. All these optimization procedures aim to minimize the maximum displacement of the first level of the platform. In brief, the steps for tuning the optimum Interval Type-2 Fuzzy Logic Controller (IT2FLC) are systematically presented in Fig. (6).

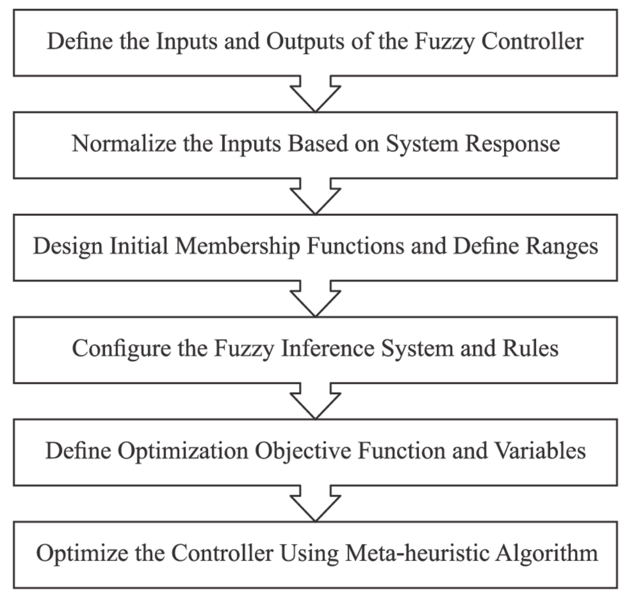

Fig. 6. Summary of the steps for tuning the optimum Interval Type-2 Fuzzy Logic Controller (IT2FLC).

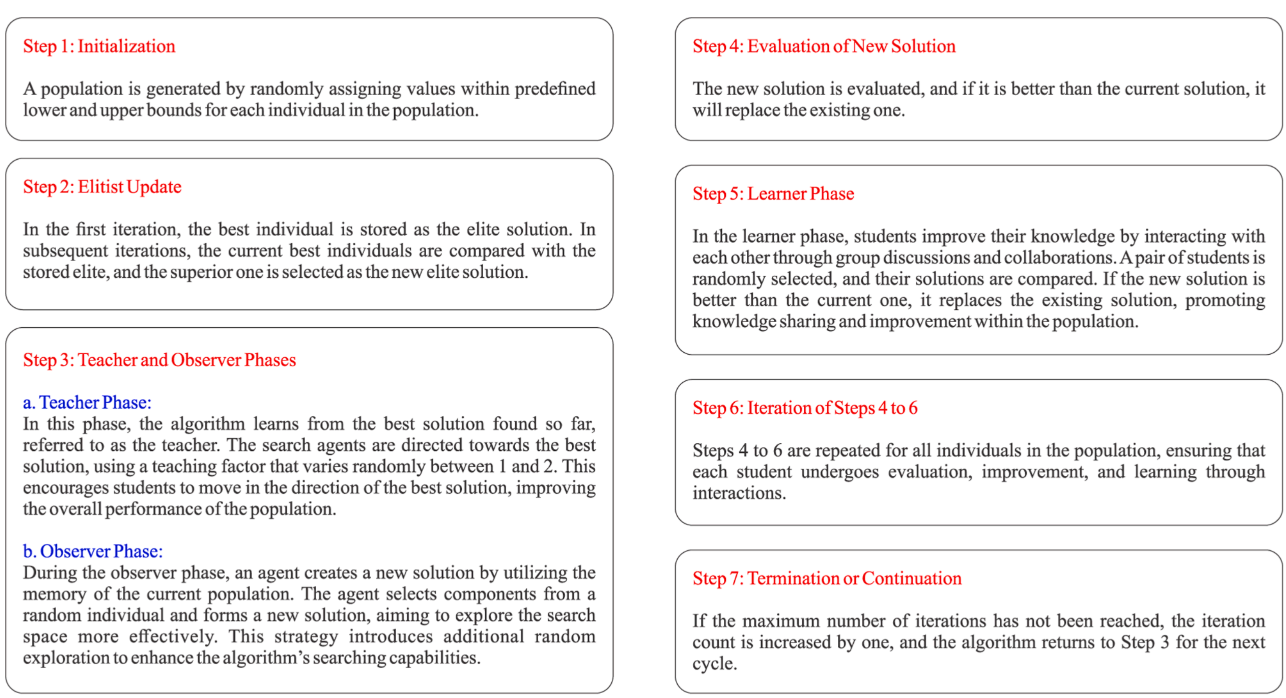

Fig. 5. Summary of the steps of the OTLBO algorithm.

4. Verification and numerical study

In the present investigation, first the nonlinear dynamic performance of the Ressalat offshore platform subjected to the concurrent influence of wind and wave-induced vibrations with varying return periods is investigated. Subsequently, a novel and appropriate control methodology to mitigate these vibrations is employed. This platform, of the jacket variety, is situated in the territorial waters of Iran within the Persian Gulf, having endured significant structural challenges in past years (Golafshani et al., 2009). To simulate the platform's behavior, a basic model with 7 dof is adopted, and its parameters are derived from three-dimensional structural modeling using ANSYS software and period equivalencing techniques (Mohajernassab et al., 2014). Table (1) presents the equivalent parameters of mass, pre-yielding stiffness, volume, and cross-sectional area of structural members at various platform levels under wave loading. Additionally, the damping matrix is computed utilizing Rayleigh damping assuming 2 % damping for the first and second vibration modes.

In the initial step, a validation process was conducted to ensure the accuracy of platform modeling using the concept of period equivalence. This process involved validating wave generation with various return periods using a novel approach and verifying the platform's analysis under linear conditions. The study by Mohajernassab et al. (Mohajernassab et al., 2017) utilized the Modified Endurance Wave Analysis (MEWA) method to apply wave loads to the Ressalat oil platform for this purpose. They employed a 7-DOF equivalent model to simulate the platform and subsequently subjected it to waves generated with different return periods. The periods of the first two vibration modes of the platform in their study for linear behavior were reported as 2.35 and 0.50 s, respectively, while our modeling efforts yielded values of 2.34 and 0.46 s, respectively. A comparison was then conducted between the platform's maximum deck displacement and the corresponding maximum base shear under wave conditions with return periods spanning 2 to 100 years. The attained results are presented in Table (2). The consistency observed between these results and those of the reference study confirms the validity of the platform modeling, wave generation, and analysis methodologies.

As detailed in Section 2, the Bouc-Wen model is utilized to simulate the hysteretic behavior of the structure under investigation. The relevant equations are thoroughly described in Section 2. For this modeling approach, the pre-yielding stiffness values corresponding to various mass levels of the structure are given in Table (1), with a post-yielding stiffness assumed to be 0.2 times these values ($\alpha_i = 0.2$) thereafter. The yield level varies according to the stiffness of each level of the platform, with the yield deformations of the first to seventh levels being 24, 22, 20, 18, 16, 14, and 12 mm, respectively. The values of other parameters related to Bouc-Wen hysteresis behavior are detailed as follows: $P_i' = 1.5$, $\lambda_i' = 0.5$, $\psi_i' = 0.5$, and $n_i' = 1$.

The loads applied to the modeled platform in this study encompass wind and wave loads having different return rates. For wave loading, six different wave scenarios are utilized, corresponding to return periods of 2, 5, 10, 20, 50, and 100 years, and the MEWA wave theory is employed for their generation. To use this theory, the significant wave height values, peak spectral period, and peak level for different return periods in the Persian Gulf are provided in Table (3). For example, Fig. (7) presents the time histories of acceleration and velocity obtained from the MEWA wave theory for two waves with return periods of 50 and 100 years, corresponding to the fifth and sixth levels of the platform. Additionally, to examine the concurrent effect of vibrational forces on the structure, a wind load proportional to the wave with different return periods is also applied. To this end, the mean and gust wind speeds related to various return periods are presented in Table (4). As described in Section 2 of the article, the NatHaz program was used to attain the history of the fluctuating wind speed. To achieve this, a duration of 1200 s is considered along with a cut-off frequency identical to the platform's fundamental frequency. According to the ASCE 7–98 code guidelines, platforms located in the ocean fall under Exposure Category D. (Jeong et al., 2019). In the following, the history of wind speed for different return periods was obtained by a combination of the fluctuating and mean wind speeds, segmented by each level of the platform. Subsequently, wind forces were calculated, considering the tributary areas for the 6th and 7th levels of the platform located above the sea as 15.6 m^2 and 74.35 m^2, respectively.

To control the vibrations of this platform, a semi-active tuned mass damper inerter (SATMDI) has been employed. An illustration of this damper is shown in Fig. (8). This damper is installed on top of the first level of the platform, with its inerter's second terminal which is connected to the 4th level. Usually, these dampers are tuned based on the primary frequency of the structure, necessitating the optimization of the initial parameters of the damper to ensure maximum efficiency (Farzam et al., 2021). The passive TMDI damper operates using four parameters, detailed in Table (5), which also lists the possible extreme values for each parameter. The optimization of these four parameters was carried out using an algorithm called the Observer-Teacher-Learner-Based Optimization (OTLBO). In this optimization process, the objective function was the reduction of the maximum inter-story drift at the first level of the platform subjected to simultaneous wind and wave excitation with a 100-year return period. The optimal values obtained from this optimization process are also provided in Table (5).

After the optimal design of the TMDI, a 1000 kN capacity Magnetorheological (MR) damper is employed to provide variable damping.

Table 1
The characteristics of various mass levels of the Ressalat jacket platform located in the Persian Gulf (Mohajernassab et al., 2014).

Ressalat platform	Level 1	Level 2	Level 3	Level 4	Level 5	Level 6	Level 7
Mass (ton)	106	129	116	105	92	63	1790
Pre-yielding Stiffness (MN/m)	179	146	146	121	106	90	38
Volume (m^3)	134	134	117	113	103	22	0
Cross-Sectional Area (m^2)	227	238	213	209	191	35	0

Table 2
Comparison of results from the linear platform modeling with the reference study.

Return period (n-year)	Maximum displacement of deck (m)		Maximum base shear (MN)	
	Reference value (Mohajernassab et al., 2017)	Present study	Reference value (Mohajernassab et al., 2017)	Present study
2	0.017	0.017	0.316	0.312
5	0.022	0.021	0.446	0.438
10	0.028	0.027	0.576	0.558
20	0.037	0.035	0.727	0.702
50	0.061	0.059	1.089	1.051
100	0.077	0.074	1.339	1.274

Table 3
Properties of Persian Gulf waves having various return periods.

Return period (n-year)	Significant wave height (m)	Peak spectral period (s)	Peak level (m)
2	2.82	4.94	2.31
5	3.62	5.59	2.96
10	4.15	5.99	3.40
20	4.67	6.35	3.82
50	5.33	6.77	4.36
100	5.83	7.10	4.77

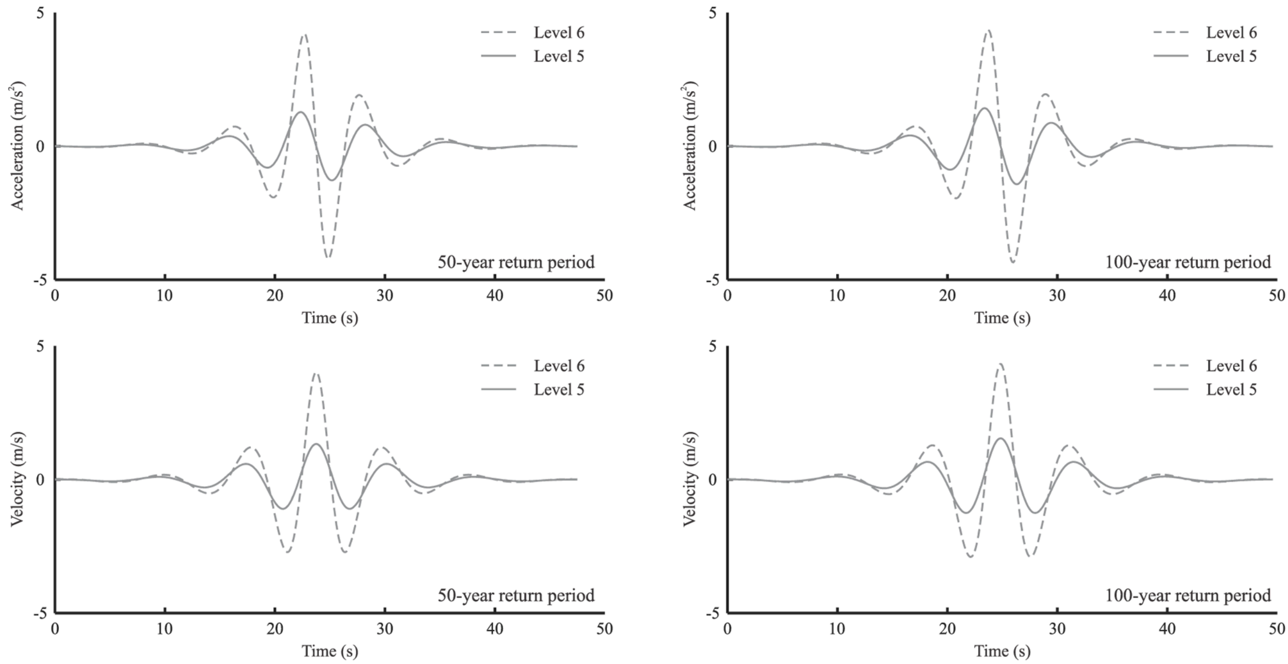

Fig. 7. Time histories of acceleration and velocity obtained from the MEWA wave theory for two waves with 50 and 100-year return periods at the fifth and sixth levels of the platform.

Table 4
The mean and gust speeds for wind with various return periods at the platform location in the Persian Gulf.

Return period (n-year)	Mean Wind Speed (m/s)	Gust Wind Speed (m/s)
2	17.47	26.59
5	19.21	29.25
10	22.10	33.70
20	22.69	34.59
50	24.45	37.25
100	27.40	41.70

Table 5
Design parameters of the TMDI along with their minimum, maximum, and optimal values.

Parameter	Definition	Minimum Value	Maximum value	Optimum value
μ	Mass ratio	0	0.02	0.0047
β	Inertance ratio	0	1	0.0261
γ	Frequency ratio	0.5	1.2	0.8014
ζ	Damping ratio	0. 1	0.8	0.2596

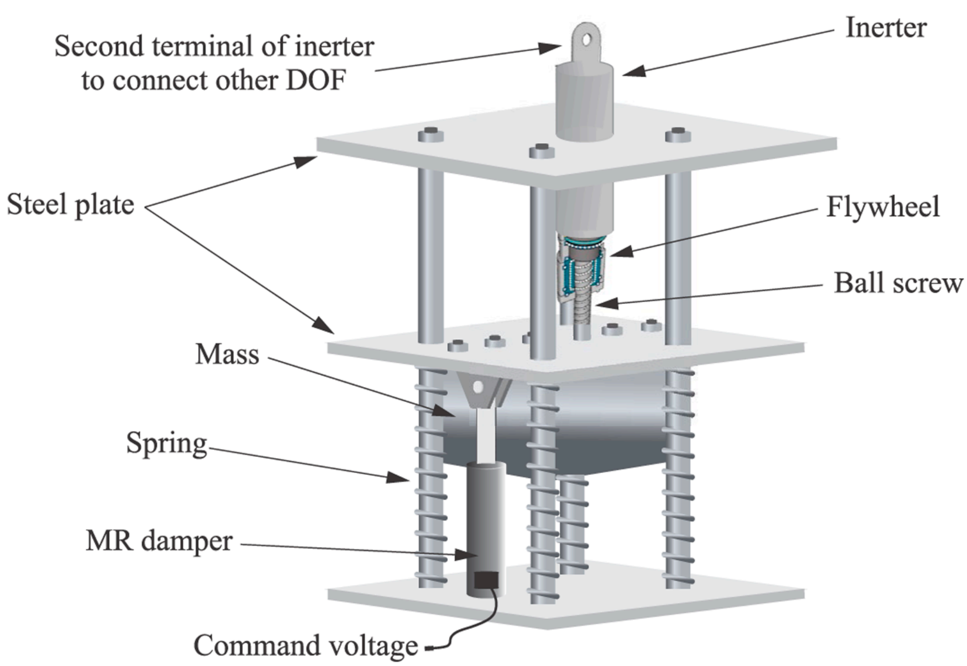

Fig. 8. Schematic view of a SATMDI damper and its components.

Table 6
Parameters of a 1000 kN capacity MR damper operating with a maximum voltage of 10 Vs (Yoshida and Dyke, 2004).

Parameter	c_{0a}	c_{0b}	α_a	α_b	n	D	ψ	T	λ
Value	4.4	44	1.0872E5	4.9616E5	1	1.2	3	50	3
Unit	N•s/cm	N•s/cm/V	N/cm	N/cm/V	–	–	1/cm	1/s	1/cm

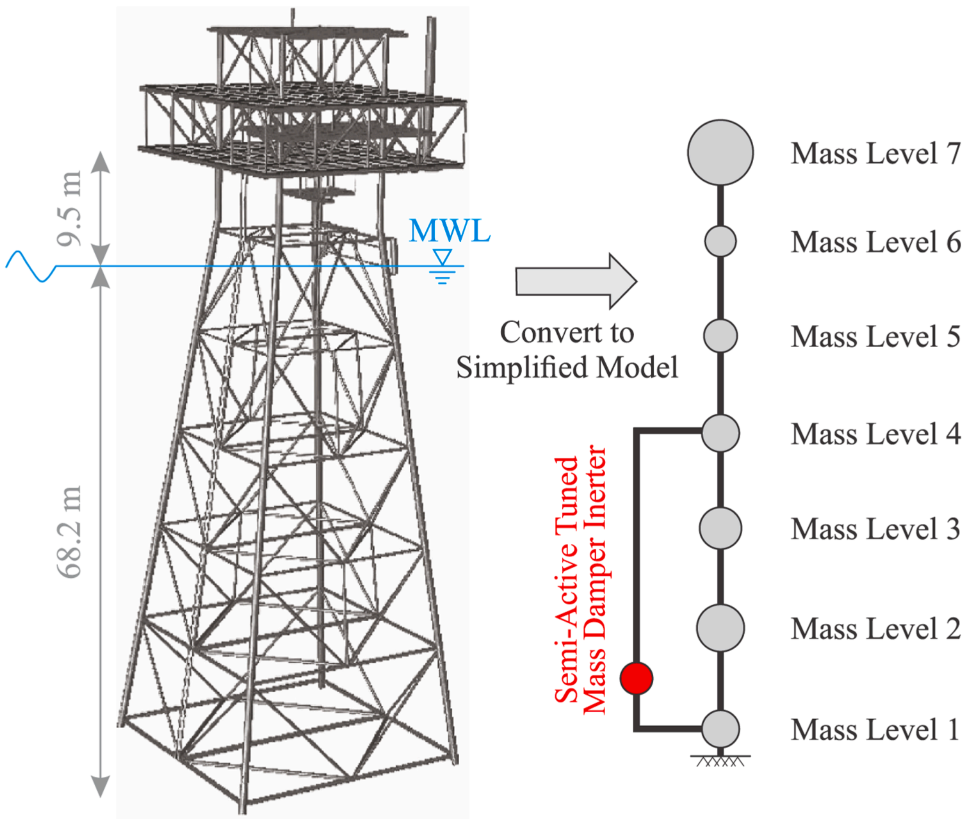

Fig. 9. Overview of the studied platform and the adopted equivalent 7-dof model, including the position of the control system.

The Bouc-Wen model is utilized to simulate the performance of the MR damper. The MR damper parameters, operating at a maximum voltage of 10 Vs, are given in Table (6). In designing the SATMDI, efforts have been made to ensure that the maximum energy dissipation occurs upon yielding, thereby significantly reducing the structural responses. For this reason, a yield deformation of 10 mm has been considered. Fig. (9) demonstrates the platform structure and its mass levels, as well as the location of the control system schematically.

An Interval Type-2 Fuzzy Logic Controller (IT2FLC) is utilized for real-time voltage computation of the MR damper. Generally, altering the voltage changes the magnetic field applied to the MR fluid, affecting its viscosity and, consequently, the resistance to fluid flow through the damper orifices. A resistance force corresponding to the applied excitation can be generated in real-time by adjusting the input voltage utilizing an appropriate controller. Thus, the design of a proper controller is critical. As explained in Section 3, the utilized controller features two inputs (i.e. the first level displacement and velocity) and one output (MR damper voltage). Five upper and lower triangular MFs are used for each input and seven for the output. The OTLBO optimization algorithm has been employed once again to determine the optimal MFs. The shapes of the optimal MFs for the inputs and outputs are shown in Fig. (10). For inputs MFs, the letters used are defined as follows: LN stands for Large Negative, N represents Negative, Z is equivalent to Zero, P specifies Positive, and LP stands for Large Positive values of inputs. Similarly, the adopted letters for outputs are as follows: EL means Extremely Low, L signifies Low, RL stands for Relatively Low, M represents Medium, RH characterizes Relatively High, H denotes High, and EH characterizes Extremely High voltage values. This optimization aims to minimize the maximum inter-story drift of the first platform level under a 100-year return period wave and wind loads. Additionally, the 25 rules for the Mamdani inference system are optimized and presented in Table (7). The optimization process adheres to the principle of symmetry.

According to the methodologies presented in Section 2, this study incorporates Fluid–Structure Interaction (FSI) and added mass effects. MATLAB/Simulink is used for modeling and analyzing the platform, as well as optimizing and controlling it, while taking FSI and added mass considerations into account. Actuator saturation is also incorporated as a constraint during the control process. The ode45 method is employed to solve the differential equations of motion and compute the relative displacements, velocities, and accelerations of the platform levels in both linear and nonlinear states.

5. Results and discussions

To conduct a comprehensive evaluation of the designed control system's efficacy in mitigating responses of the non-linear jacket platform under simultaneous wave and wind loading, diverse responses were scrutinized. Initially, in Fig. (11), the relationship between restoring force and inter-story drift is depicted for the first, fourth, and seventh levels of the structure under three simultaneous wave and wind loadings with return periods of 2, 10, and 100 years in uncontrolled conditions, illustrating the non-linear behavior of the studied structure.

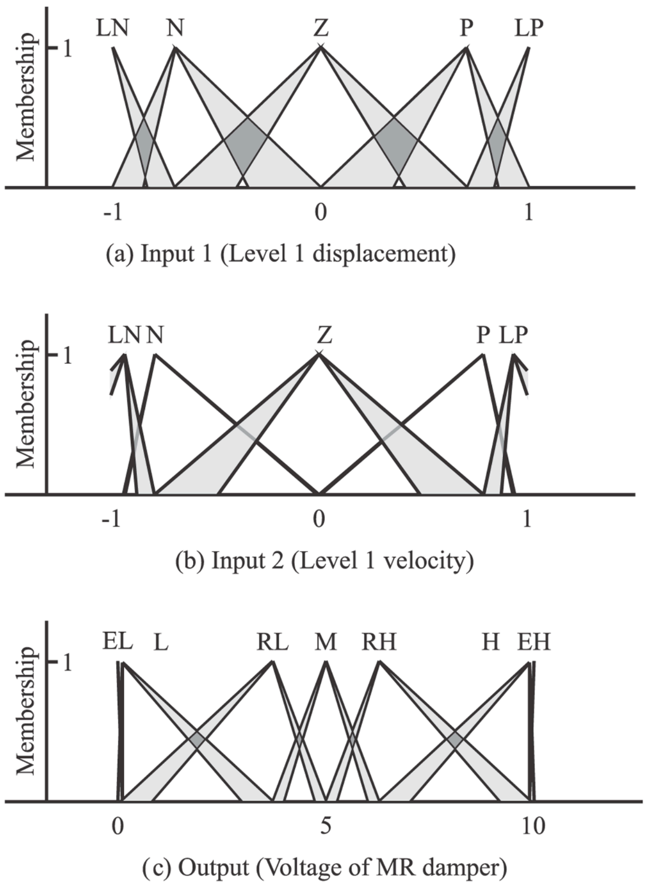

Fig. 10. Optimal MFs for the inputs and output of the interval type-2 fuzzy controller.

Table 7
Optimal rules for the interval type-2 fuzzy controller.

Velocity	Displacement				
	LN	N	Z	P	LP
LN	EL	RH	M	RH	RL
N	RH	EL	M	EL	RH
Z	M	M	M	L	RL
P	RH	EL	L	M	M
LP	RL	RH	RL	M	M

A comparison of the hysteresis curves presented in this figure reveals that with increasing loading return periods, both inter-story drift and restoring force escalate, resulting in larger hysteresis curves for longer loading return periods. Additionally, a noteworthy observation from this figure is the reduction in hysteresis curves for upper platform levels compared to lower ones. Therefore, based on these considerations, the placement of the SATMDI damper at the top of the first level and the selection of the response of the first level as the objective function in the optimization process have been justified. Essentially, this study aims to minimize the largest hysteresis curve observed, belonging to the first level of the platform under a 100-year return period loading. By opting for this objective, the inter-story drift at the first level experiences the most significant reduction, leading to a substantial decrease in structural displacement.

In the following, a comparison between the hysteresis curves of the first level of the platform in uncontrolled and controlled conditions is performed in Fig. (12) for loading with return periods of 2, 5, 10, 20, 50, and 100 years, with uncontrolled curves shown in gray and controlled curves in red. The results indicate that the application of the control system causes the structural behavior to transition from non-linear to linear under all loading conditions, resulting in a substantial decrease in inter-story drift and restoring force for all hysteresis curves. To quantitatively compare different scenarios, the areas under the uncontrolled and controlled hysteresis curves are shown in gray and red within each figure, representing the energy dissipated in joules. In the absence of a control system, the structure is responsible for dissipating energy, leading to plastic deformation and potential structural damage. However, by employing the designed control system, the energy dissipation responsibility is shifted away from the structure; The damper absorbs a substantial amount of the energy, maintaining the structure in the elastic range and preventing any damage. For instance, when subjected to a 100-year return period loading scenario, the structure dissipates 1.0628E8 joules of energy. With the implementation of the control system, this value decreases to 2.9349E5 joules, with the remaining being dissipated by the damper. In other words, the control system is responsible for dissipating >99 % of the energy, thereby preventing a substantial portion of the incoming energy from affecting the structure. This percentage of reduction remains consistent for all loading conditions, indicating the stable and effective performance of the designed control system under various loading scenarios.

In Fig. (13), the time history of inter-story drift at the first level under loadings with various return periods is depicted for both uncontrolled and controlled conditions, with uncontrolled shown in gray and controlled in red, for the initial 35 s of vibration. It is evident from Fig. (13) that the inter-story drift increases with longer loading return periods. In this figure, the yield drift is depicted in black on each time history plot. When the drift of the structure exceeds the designated range, it signifies that the structure has entered the plastic deformation region. Analysis of this figure reveals that, in the uncontrolled state, the structure frequently enters the plastic region and exhibits nonlinear behavior. However, with the addition of the control system, this nonlinear behavior is entirely transformed into linear behavior. Therefore, the SATMDI control system, equipped with the optimized controller, effectively maintains the structure's response within the elastic range, nearly eliminating the risk of non-linear damage and yielding. Consequently, the high capability of the proposed control system in improving the performance of the non-linear platform under wave and wind loading can be inferred.

Inter-story drift and absolute acceleration are pivotal responses when evaluating the vibrations of offshore platforms, critical for maintaining structural safety and equipment integrity. While previous findings have shown a general reduction in inter-story drift, Fig. (14) offers a detailed analysis of the reduction in inter-story drift at the first level of the platform, as well as the absolute acceleration, for various return period loadings. In Figure (14a), the reduction in the maximum responses is illustrated, while Figure (14b) depicts the reduction in the root mean square (RMS) of the responses. As an example, in the case of a 100-year return period loading, the maximum value of inter-story drift and also the absolute acceleration are reduced by 91.61 % and 83.04 %, respectively, while the RMS of these responses is reduced by 89.90 % and 83.05 %, respectively. On average, across all loading conditions, the maximum inter-story drift and absolute acceleration responses are reduced by 90 % and 83 %, respectively. Furthermore, the RMS values of these responses are decreased by 89 % and 83 %, respectively. The most significant reduction among all responses is associated with the maximum inter-story drift at the first level subjected to a 100-year return period loading, aligning with the optimization objectives of the control system design. Overall, the results show that the implemented control system not only reduces the platform's maximum response values but also effectively mitigates its responses throughout the entire vibration duration.

In Table (8), a comparison is made between the uncontrolled and controlled responses (using various methods) of the first and top levels of the platform under loading with a return period of 100 years in both linear and nonlinear states. This table shows that when the structure

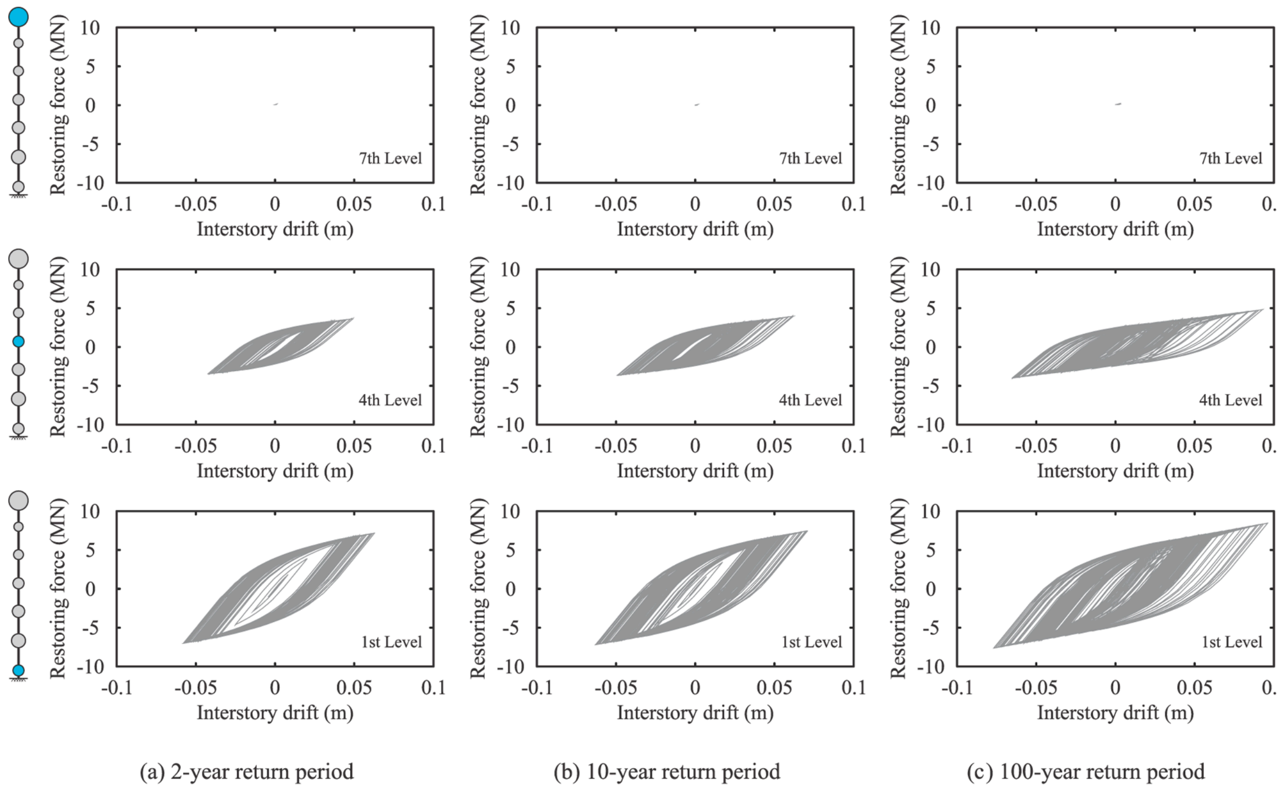

Fig. 11. Hysteresis curves for the 1st, 4th, and 7th levels of the platform with non-linear behavior in uncontrolled conditions when subjected to: a) a 2-year return period loading; b) a 10-year return period loading; c) a 100-year return period loading.

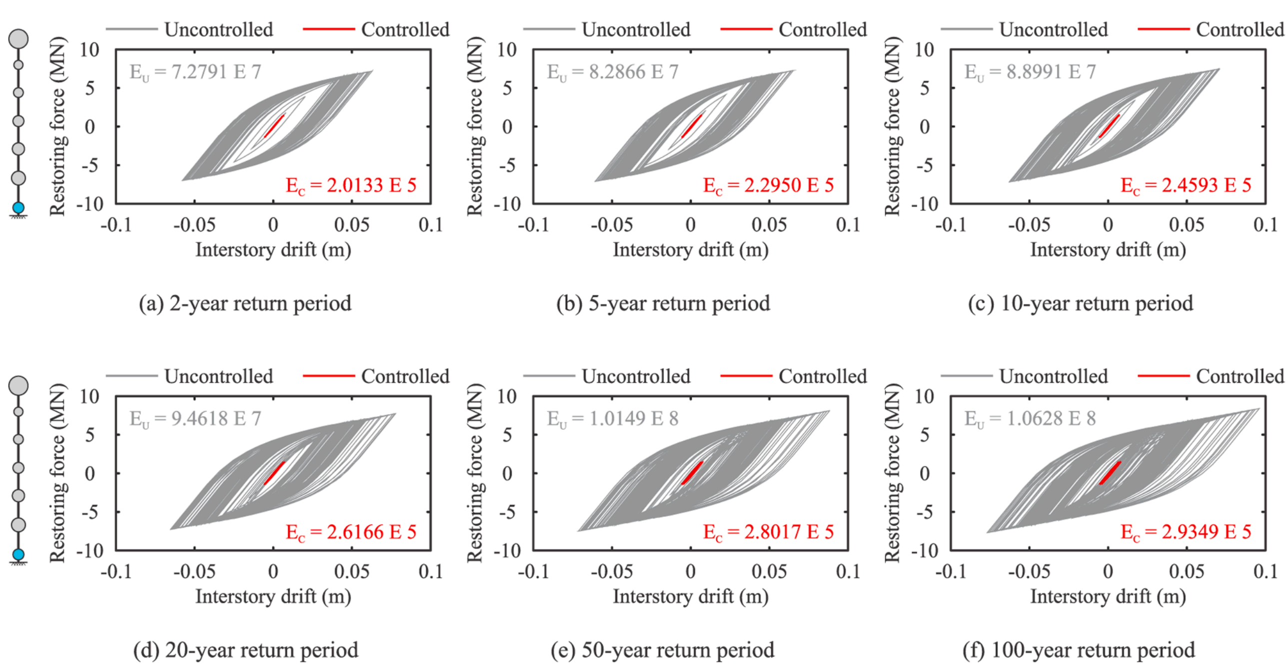

Fig. 12. Hysteresis curves for the 1st level of the platform with non-linear behavior in uncontrolled and controlled conditions for loadings with different return periods, along with the areas enclosed by each curve.

enters the nonlinear domain, the inter-story drift of the first level increases, which nearly leads to the collapse of the structure. However, this value decreases at the deck level, which can occur for various reasons. For instance, as the structure transitions to nonlinear behavior, significant energy dissipation at the lower levels reduces the energy transmitted to the upper levels, resulting in decreased deformation in those levels. The table also provides a comparison of the controlled responses using different approaches. For example, the TMDI tuned for the nonlinear state reduces the inter-story drift of the first level by 87 %, whereas in the linear state, it increases the response. This discrepancy arises from its lack of tuning for the linear condition. By converting this damper into a semi-active system, the adverse impact is mitigated,

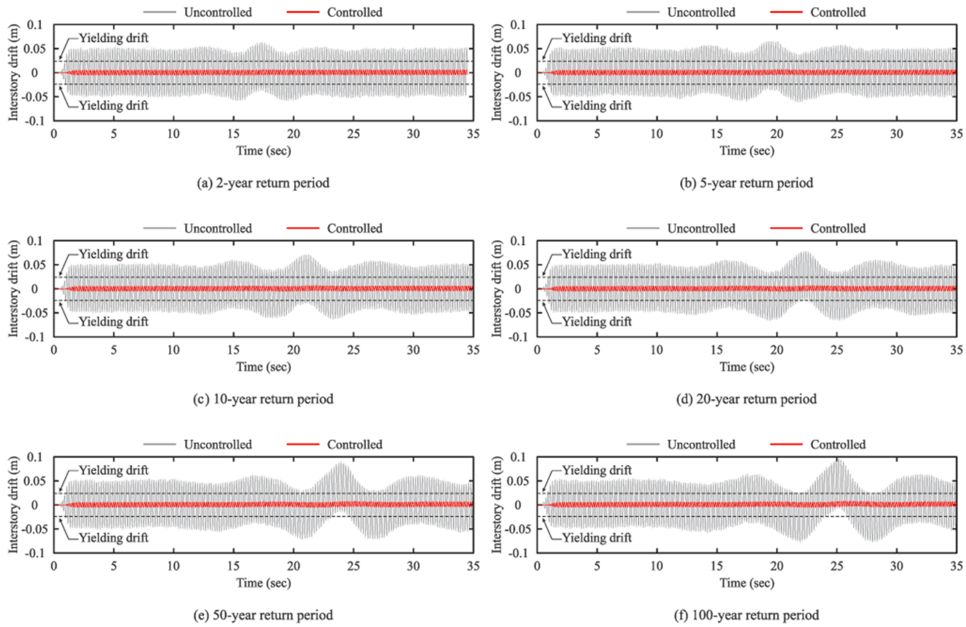

Fig. 13. Time history of inter-story drift response at the first level of the platform in both uncontrolled and controlled conditions, categorized by different loadings with various return periods.

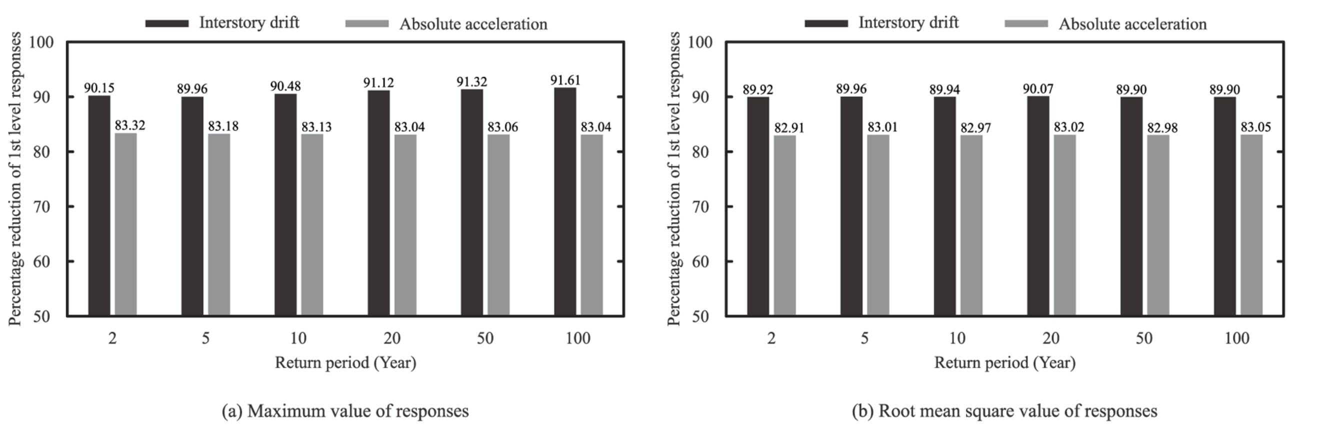

Fig. 14. Reduction in inter-story drift and absolute acceleration responses at the first level of the platform subjected to loadings with various return periods. a) Maximum values of responses; b) RMS of responses.

Table 8
Uncontrolled and controlled responses of the platform's first and top levels under 100-year return period loading in linear and nonlinear states.

Control Strategy	Structure Level	Inter-story drift (m)	
		Linear	Nonlinear
Uncontrolled	First Level	0.0073	0.0961
	Deck Level	0.0121	0.0031
TMDI	First Level	0.0313	0.0122
	Deck Level	0.0402	0.0030
TMD	First Level	0.0313	6.2
	Deck Level	0.0402	0
SATMDI	First Level	0.0171	0.0080
	Deck Level	0.0198	0.0014

achieving a 91.6 % reduction in the first-level response in the nonlinear state, highlighting the superior performance of the proposed control strategy compared to the TMDI. Additionally, the table presents the responses of the TMD damper, calculated using the same parameters as the TMDI. The responses of TMD and TMDI are identical in the linear state; however, they exhibit completely different behaviors in the

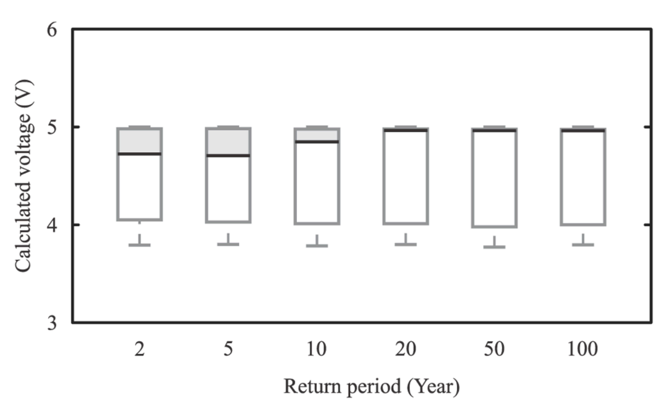

Fig. 15. Boxplot illustrating the voltage distribution generated by the designed control system under various loading return periods.

nonlinear state. Specifically, the TMD damper leads to a substantial increase in the inter-story drift of the first level, to the extent that the structure completely collapses, resulting in a zero inter-story drift at the deck level. From this comparison, it can be concluded that despite the similar performance of these two dampers in the linear state, the addition of the inerter to the control system in the nonlinear state significantly improves the structural condition, transforming the control system's behavior from detrimental to effective.

Finally, the boxplot diagram presented in Fig. (15) conducts a statistical analysis and dispersion assessment of the voltage produced by the optimized IT2FLC controller for loadings with different return periods. Each box in this diagram represents the distribution of calculated voltages for a specific return period. Additionally, each box indicates the interquartile range (IQR), with the lower and upper edges respectively representing the 25th and 75th percentiles. Moreover, the ends of the whiskers denote the minimum and maximum voltage values over time during excitation, while the horizontal line within each box, depicted in black, represents the median of the calculated voltages for that return period. Across almost all loadings, consistent maximum and minimum controlled voltage values are observed, along with a consistent IQR range, indicating a uniform distribution of 50 % of the intermediate voltage range resulting from IT2FLC. This criterion is crucial as it remains independent of initial and final data, which may exhibit significant variations and solely evaluates the intermediate data range. Furthermore, the standard deviation of the voltage during excitations with different return periods remains approximately constant. The results also indicate that as the loading period increases, the median voltage produced by the controller during excitation increases. The highest median is observed for the loading scenario with a 100-year return period. Additionally, in all examined cases, the voltage distribution displays a negative skewness, intensifying as the return period loading increases. Nevertheless, in none of the examined cases was it necessary to utilize the full capacity of the control system, underscoring the robust capability of the designed control system to handle even more challenging loading scenarios. This aspect is also important for extending the lifespan of the control system and minimizing its wear and tear. Furthermore, taking the aforementioned points into account, it can be inferred that despite certain implementation challenges like time delays, the designed controller can improve the platform's dynamic performance offline by applying a constant voltage.

6. Conclusion

This study delves into evaluating the performance of the SATMDI damper in mitigating vibrations of the Ressalat offshore platform, characterized by nonlinear behavior under the influence of wind and wave loadings with varying return periods. Nonlinear behavior is captured through the utilization of the Bouc-Wen hysteresis curve. Additionally, the IT2FLC controller is employed to dynamically compute the control voltage for the damper in real-time, aligning with the input excitation. Parameter optimization of the designed control system is facilitated through the application of the OTLBO optimization algorithm. To comprehensively evaluate the efficiency of the damper and controller, a range of structural responses is presented, encompassing maximum and RMS inter-story drift, as well as absolute acceleration. Furthermore, hysteresis curves of the structure are compared under both uncontrolled and controlled conditions. The findings are meticulously evaluated and interpreted, encompassing both qualitative and quantitative analyses. The main conclusions derived from the present study can be summarized as follows:

- As the return period of loading increases, both inter-story drift and restoring force intensify, consequently leading to the formation of larger hysteresis curves. Notably, the largest hysteresis curve corresponds to the lowest platform level, while the smallest is associated with the platform deck.
- The introduction of the proposed control system results in a transition of structural behavior from nonlinear to linear across all loadings and scenarios, significantly reducing inter-story drift and restoring force.
- In the absence of a control system, the structure bears the burden of energy dissipation, leading to plastic deformation. However, with the integration of the control system, the participation of the structure in energy dissipation reduces, preserving the structure in a linear state. The substantial reduction (by 99 %) in the area under the hysteresis curve across all loadings underscores the efficacy of the designed control system in dissipating a significant share of the input energy, while just a negligible amount is imparted to the structure. The consistency of this reduction across various loadings highlights the stability and reliable performance of the developed control system.
- On average, across various loadings, maximum inter-story drift and the platform absolute acceleration decrease by 90 % and 83 %, respectively, with their RMS also diminishing by 89 % and 83 %, respectively. This highlights the efficacy of the developed control system in not only reducing maximum platform response values but also maintaining excellent performance over time during excitation.
- The control system's performance improves by increasing the return period of the loading, with maximal effectiveness observed in the case of a 100-year return period loading, though this may be attributed to the optimization objectives pursued in this study.
- Under various loading periods, the median of the required voltage by the control system increases, accompanied by intensified negative skewness. However, overall, the minimum and maximum voltage values during excitation remain consistent across all loadings, hovering around 3.8 and 5 Vs, respectively. This underscores the system's ability to enhance the service life of the control system and its readiness to handle more demanding loading conditions.

In summary, the results underscore the effectiveness of the optimized SATMDI + IT2FLC control system in averting nonlinear behavior and preventing structural damage. Moreover, its significant advantage over passive systems lies in its ability to effectively dissipate input energy into the structure, highlighting the importance of determining damper parameters online in proportion to input vibrations. Lastly, the employed nonlinear modeling technique holds promise for garnering considerable attention in various studies.

Despite the promising results and the high effectiveness of the proposed damper in mitigating vibrations of offshore platforms under nonlinear conditions, it is essential to address the limitations of this study. For instance, the Bouc-Wen model was employed to represent nonlinear behavior. While widely accepted by researchers, this model may not fully capture the complexity of the real structure's nonlinear behavior in certain scenarios. Furthermore, this study focused on a specific structural configuration, highlighting the need for further analytical and experimental investigations to generalize the findings.

CRediT authorship contribution statement

Seyyed Ali Mousavi Gavgani: Writing – original draft, Software, Data curation, Formal analysis, Investigation, Resources, Validation, Visualization. **Seyed Hossein Hosseini Lavassani:** Writing – review & editing, Supervision, Project administration, Methodology, Conceptualization. **Gebrail Bekdaş:** Writing – review & editing, Supervision, Visualization.

Declaration of competing interest

The authors declare that they have no known competing financial interests or personal relationships that could have appeared to influence the work reported in this paper.

Funding

This research was not funded by any organization or company.

References

Abdel-Rohman, M., 1996. Structural control of a steel jacket platform. Struct. Engineer. Mechan. 4 (2), 125–138.
Al-Ghazali, A.S., Shariatmadar, H., 2021. Hybrid active control of adjacent buildings interconnected by viscous dampers utilizing type-2 fuzzy controller considering soil-structure interaction. Structures. Elsevier.
Baheti, A.S., Matsagar, V.A., 2022. Wind and seismic response control of dynamically similar adjacent buildings connected using magneto-rheological dampers. Infrastructures 7 (12), 167.
Banerjee, S., Ghosh, A., Matsagar, V.A., 2022. Optimum design of nonlinear tuned mass damper for dynamic response control under earthquake and wind excitations. Struct. Control Health Monitor. 29 (7), e2960.
Bhattacharya, S., Dalui, S.K., 2022. Effect of tuned mass damper in wind-induced response of "V" plan-shaped tall building. Struct. Design Tall Special Build. 31 (9), e1931.
Bigdeli, Y., Kim, D., Chang, S., 2014. Vibration control of 3D irregular buildings by using developed neuro-controller strategy. Struct. Engineer. Mech. 49 (6), 687–703.
Chen, M.Z., et al., 2009. The missing mechanical circuit element. IEEE Circuit. Syst. Magaz. 9 (1), 10–26.
Cheong, F., Lai, R., 2000. Constraining the optimization of a fuzzy logic controller using an enhanced genetic algorithm. IEEE Transac. Syst., Man, Cybernet., Part B (Cybernetics) 30 (1), 31–46.
Dai, J., et al., 2021. Optimal design of tuned mass damper inerter with a Maxwell element for mitigating the vortex-induced vibration in bridges. Mech. Syst. Signal. Process. 148, 107180.
Dastan Diznab, M.A., et al., 2016. Wave endurance time: a new concept for structural assessment under extreme waves. Proc. Institut. Mech. Engineers, Part M 230 (2), 364–377.
De Angelis, M., Perno, S., Reggio, A., 2012. Dynamic response and optimal design of structures with large mass ratio TMD. Earthq. Eng. Struct. Dyn. 41 (1), 41–60.
DeFranco, S., et al., 2004. Eugene Island 322′A'drilling platform decommissioning after hurricane lilli. In: Offshore Technology Conference. OTC.
Den Hartog, J., 1956. Mechanical Vibrations, 4th ed. Dover Publications.
Djerouni, S., et al., 2021. Optimum double mass tuned damper inerter for control of structure subjected to ground motions. J. Build. Engineer. 44, 103259.
Du, Z., Kao, Y., Park, J.H., 2020. New results for sampled-data control of interval type-2 fuzzy nonlinear systems. J. Franklin. Inst. 357 (1), 121–141.
Elias, S., Matsagar, V., Datta, T.K., 2019. Along-wind response control of chimneys with distributed multiple tuned mass dampers. Struct. Control Health Monitor. 26 (1), e2275.
Enferadi, M.H., Ghasemi, M.R., Shabakhty, N., 2019. Wave-induced vibration control of offshore jacket platforms through SMA dampers. Appl. Ocean Res. 90, 101848.
Fahimi Farzam, M., Alinejad, B., Mousavi Gavgani, S.A., 2021. statistical performance of semi-active controlled 10-storey linear building using mr damper under earthquake motions. Amirkabir J. Civil Engineer. 53 (4), 1571–1590.
Farzam, M.F., et al., 2020. Current trends in the optimization approaches for optimal structural control. Adv. Struct. Engineer.—Optimiz. 133–179.
Farzam, M.F., et al., 2021. Control of a jacket platform under wave load using ATMD and optimization by HSA. In: Proceedings of 6th International Conference on Harmony Search, Soft Computing and Applications: ICHSA 2020, Istanbul. Springer.
Gavgani, S.A.M., Jalali, H.H., Farzam, M.F., 2021. Semi-active control of jacket platforms under wave loads considering fluid-structure interaction. Appl. Ocean Res. 117, 102939.
Giaralis, A., Marian, L., 2016. Use of inerter devices for weight reduction of tuned mass-dampers for seismic protection of multi-story building: the Tuned mass-damper-interter (TMDI). In: Active and Passive Smart Structures and Integrated Systems 2016. SPIE.
Giaralis, A., Petrini, F., 2017. Optimum design of the tuned mass-damper-inerter for serviceability limit state performance in wind-excited tall buildings. Procedia Eng. 199, 1773–1778.
Giaralis, A., Taflanidis, A., 2018. Optimal tuned mass-damper-inerter (TMDI) design for seismically excited MDOF structures with model uncertainties based on reliability criteria. Struct. Control Health Monitor. 25 (2), e2082.
Golafshani, A.A., Tabeshpour, M.R., Komachi, Y., 2009. FEMA approaches in seismic assessment of jacket platforms (case study: ressalat jacket of Persian gulf). J. Constr. Steel. Res. 65 (10–11), 1979–1986.
Hoang, N., Fujino, Y., Warnitchai, P., 2008. Optimal tuned mass damper for seismic applications and practical design formulas. Eng. Struct. 30 (3), 707–715.
Hu, Y., et al., 2018. Load mitigation for a barge-type floating offshore wind turbine via inerter-based passive structural control. Eng. Struct. 177, 198–209.
Hwang, J.-S., Kim, J., Kim, Y.-M., 2007. Rotational inertia dampers with toggle bracing for vibration control of a building structure. Eng. Struct. 29 (6), 1201–1208.
Ikhouane, F., Rodellar, J., 2007. Systems With hysteresis: analysis, Identification and Control Using the Bouc-Wen model. John Wiley & Sons.
Jalali, H.H., et al., 2023. Semi-active control of buildings using different control algorithms considering SSI. J. Build. Engineer. 67, 105956.
Jeong, S., Lee, Y.-J., Sim, S.-H., 2019. Serviceability assessment method of stay cables with vibration control using first-passage probability. Math. Probl. Eng. 2019 (1), 4138279.
John, E.D., Wagg, D.J., 2019. Design and testing of a frictionless mechanical inerter device using living-hinges. J. Franklin. Inst. 356 (14), 7650–7668.
Kaimal, J.C., et al., 1972. Spectral characteristics of surface-layer turbulence. Quart. J. Royal Meteorolog. Soc. 98 (417), 563–589.
Kaiser, M.J., Pulsipher, A.G., 2007. The impact of weather and ocean forecasting on hydrocarbon production and pollution management in the Gulf of Mexico. Energy Policy 35 (2), 966–983.
Karnik, N.N., Mendel, J.M., 1998. Type-2 fuzzy logic systems: type-reduction. In: SMC'98 Conference Proceedings. 1998 IEEE International Conference on Systems, Man, and Cybernetics (Cat. No. 98CH36218). Ieee.
Kelessidis, V., 2009. Challenges for very deep oil and gas drilling will there ever be a depth limit. In: third AMIREG international conference: assessing the footprint of resource utilization and hazardous waste management.
Kwon, D., Kareem, A., 2006. NatHaz on-line wind simulator (NOWS): simulation of Gaussian multivariate wind fields. NatHaz Model. Labor. Rep.
Lavassani, S.H.H., Gavgani, S.A.M., Doroudi, R., 2023. Optimal control of jacket platforms vibrations under the simultaneous effect of waves and earthquakes considering fluid-structure interaction. Ocean Engineer. 280, 114593.
Lazar, I., Neild, S., Wagg, D., 2014a. Using an inerter-based device for structural vibration suppression. Earthq. Eng. Struct. Dyn. 43 (8), 1129–1147.
Lazar, I.F., Neild, S.A., Wagg, D.J., 2014b. Design and performance analysis of inerter-based vibration control systems. In: Dynamics of Civil Structures, Volume 4: Proceedings of the 32nd IMAC, A Conference and Exposition on Structural Dynamics, 2014. Springer.
Ma, R., et al., 2023. Inerter-based damping isolation system for vibration control of offshore platforms subjected to ground motions. Ocean Engineer. 280, 114726.
Ma, R., Bi, K., Hao, H., 2018. Mitigation of heave response of semi-submersible platform (SSP) using tuned heave plate inerter (THPI). Eng. Struct. 177, 357–373.
Ma, R., Bi, K., Hao, H., 2020a. Using inerter-based control device to mitigate heave and pitch motions of semi-submersible platform in the shallow sea. Eng. Struct. 207, 110248.
Ma, R., Bi, K., Hao, H., 2020b. Heave motion mitigation of semi-submersible platform using inerter-based vibration isolation system (IVIS). Eng. Struct. 219, 110833.
Ma, R., Bi, K., Hao, H., 2021. Inerter-based structural vibration control: a state-of-the-art review. Eng. Struct. 243, 112655.
Marian, L., Giaralis, A., 2014. Optimal design of a novel tuned mass-damper–inerter (TMDI) passive vibration control configuration for stochastically support-excited structural systems. Probabil. Engineer. Mech. 38, 156–164.
Matta, E., De Stefano, A., 2009. Seismic performance of pendulum and translational roof-garden TMDs. Mech. Syst. Signal. Process. 23 (3), 908–921.
Mohajernasab, S., et al., 2014. Application of New-wave theory in the Endurance Wave method to assess offshore structures under the Persian Gulf wave conditions. J. Marine Engineer. 9 (18), 71–82.
Mohajernassab, S., et al., 2017. Modification of endurance wave analysis based on New-wave theory. Ship. Offshore Struct. 12 (3), 330–340.
Moutinho, C., 2012. An alternative methodology for designing tuned mass dampers to reduce seismic vibrations in building structures. Earthq Eng. Struct. Dyn. 41 (14), 2059–2073.
Ok, S.-Y., et al., 2007. Semi-active fuzzy control of cable-stayed bridges using magneto-rheological dampers. Eng. Struct. 29 (5), 776–788.
Paganie, D. *Ike topples old platforms*. 2008; Available from: (https://www.offshore-mag.com/subsea/article/16761720/gulf-of-mexico). [accessed: 2024-05-10].
Park, Y.J., Cho, H.S., Cha, D.H., 1995. Genetic algorithm-based optimization of fuzzy logic controller using characteristic parameters. In: Proceedings of 1995 IEEE International Conference on Evolutionary Computation. IEEE.
Pietrosanti, D., De Angelis, M., Giaralis, A., 2021. Experimental seismic performance assessment and numerical modelling of nonlinear inerter vibration absorber (IVA)-equipped base isolated structures tested on shaking table. Earthq. Eng. Struct. Dyn. 50 (10), 2732–2753.
Pourzeynali, S., Lavasani, H., Modarayi, A., 2007. Active control of high rise building structures using fuzzy logic and genetic algorithms. Eng. Struct. 29 (3), 346–357.
Quaranta, G., Mollaioli, F., Monti, G., 2016. Effectiveness of design procedures for linear TMD installed on inelastic structures under pulse-like ground motion. Earthquake. Struct. 10 (1), 239–260.
Rp2A-Wsd, A, 2007. American Petroleum Institute Recommended Practice For Planning, Designing and Constructing Fixed Offshore Platforms—Working Stress Design. American Petroleum Institute, Washington.
Ruiz, R., et al., 2018. Risk-informed optimization of the tuned mass-damper-inerter (TMDI) for the seismic protection of multi-storey building structures. Eng. Struct. 177, 836–850.
Saitoh, M., 2012. On the performance of gyro-mass devices for displacement mitigation in base isolation systems. Struct. Control Health Monitor. 19 (2), 246–259.
Shahrouzi, M., Aghabaglou, M., Rafiee, F., 2017. Observer-teacher-learner-based optimization: an enhanced meta-heuristic for structural sizing design. Struct. Engineer. Mech., An Int'l J. 62 (5), 537–550.
Simiu, E., 1974. Wind spectra and dynamic alongwind response. J. Struct. Divis. 100 (9), 1897–1910.
Singh, A.K., et al., 2022. Intelligent control of irrigation systems using fuzzy logic controller. Energies. (Basel) 15 (19), 7199.
Singh, M.P., Singh, S., Moreschi, L.M., 2002. Tuned mass dampers for response control of torsional buildings. Earthq. Eng. Struct. Dyn. 31 (4), 749–769.
Smith, M.C., 2002. Synthesis of mechanical networks: the inerter. IEEe Trans. Automat. Contr. 47 (10), 1648–1662.
Soong, T.T. and G.F. Dargush, *Passive energy dissipation systems in structural engineering.* (No Title), 1997.

Su, N., et al., 2024. Hybrid analytical H-norm optimization approach for dynamic vibration absorbers. Int. J. Mech. Sci. 264, 108796.
Su, N., Xia, Y., Peng, S., 2022. Filter-based inerter location dependence analysis approach of Tuned mass damper inerter (TMDI) and optimal design. Eng. Struct. 250, 113459.
Sun, H., et al., 2019. Exact H2 optimal solutions to inerter-based isolation systems for building structures. Struct. Control Health Monitor. 26 (6), e2357.
Temimi, H., et al., 2016. Time-delay effects on controlled seismically excited linear and nonlinear structures. Int. J. Struct. Stabil. Dyn. 16 (07), 1550031.
Wang, F.-C., et al., 2009. The performance improvements of train suspension systems with mechanical networks employing inerters. Vehicle Syst. Dyn. 47 (7), 805–830.
Wang, F.-C., Hong, M.-F., Lin, T.-C., 2011. Designing and testing a hydraulic inerter. Proceed. Institut. Mechan. Engineers, Part C 225 (1), 66–72.
Wang, J.-F., Lin, C.-C., 2005. Seismic performance of multiple tuned mass dampers for soil–irregular building interaction systems. Int. J. Solids. Struct. 42 (20), 5536–5554.
Wittig, L.E., Sinha, A.K., 1975. Simulation of multicorrelated random processes using the FFT algorithm. J. Acoust. Soc. Am. 58 (3), 630–634.
Xu, T., Li, Y., Leng, D., 2023. Mitigating jacket offshore platform vibration under earthquake and ocean waves utilizing tuned inerter damper. Bull. Earthq. Eng. 21 (3), 1627–1650.
Yang, J., Agrawal, A., Chen, S., 1996. Optimal polynomial control for seismically excited non-linear and hysteretic structures. Earthq. Eng. Struct. Dyn. 25 (11), 1211–1230.
Yoshida, O., Dyke, S.J., 2004. Seismic control of a nonlinear benchmark building using smart dampers. J. Eng. Mech. 130 (4), 386–392.
Yuan, Z.-Q., et al., 2024. Synchronous identification of nonlinear structural parameters and unknown external excitation based on improved UKF. Eng. Struct. 298, 117094.
Zadeh, L.A., 1975. The concept of a linguistic variable and its application to approximate reasoning—II. Inf. Sci. (Ny) 8 (4), 301–357.
Zhang, R., et al., 2020. Damping enhancement principle of inerter system. Struct. Control Health Monitor. 27 (5), e2523.
Zhao, L., Chang, Z., Zheng, Z., 2023. The vibration mitigation of jacket offshore platform based on inerter nonlinear energy sink. Ocean Engineer. 280, 114943.
Zhu, H., et al., 2019. Mechanical and energy-harvesting model for electromagnetic inertial mass dampers. Mech. Syst. Signal. Process. 120, 203–220.